Discrete Stiffness Tailoring: Optimised design and testing of minimum mass stiffened panels

L.E. Culliford[a,*], C. Scarth[a], T. Maierhofer[a], R. Jagpal[a], A.T. Rhead[a], R. Butler[a]

[a] *Materials and Structures Research Centre, Department of Mechanical Engineering, University of Bath, Bath, United Kingdom*

Abstract

Discrete Stiffness Tailoring (DST) is a novel manufacturing concept where stiffness tailoring is achieved using discrete changes in ply angle to favourably redistribute stresses. Resulting performance increases can be exploited to potentially achieve lightweight rapidly manufacturable structures, uninhibited by the minimum tow-turning radii which limit continuous fibre steering approaches. An efficient two-stage optimisation routine is implemented to design a DST minimum-mass stiffened aircraft wing panel subject to buckling and manufacturing feasibility constraints. The panel is manufactured and compression tested to failure, extending the DST design concept to component level for the first time. A weight reduction of 14.4% is achieved compared to a constant stiffness optimum, through redistribution of load to the stiffener region. The optimum design removes material from the skin, between stiffeners. Experimentally, the optimised tailored panel achieved a buckling load, without failure, within 5% of that predicted, validating both the methodology and modelling.

Keywords: buckling, optimisation, laminate design, manufacture

Nomenclature

$\boldsymbol{\epsilon}^0$	Mid-plane strain vector	h_{st}	Stiffener height
$\boldsymbol{\kappa}$	Mid-plane plate curvature vector	N_x	Design in-plane loading
$\boldsymbol{M}$	Moment vector	r_{st}	Outer radius for stiffener
$\boldsymbol{N}$	In-plane stress vector	t	Laminate thickness
ℓ	Effective panel length	$w_i^{A,D}$	Weighting functions
$\epsilon_{\max}$	Maximum strain allowable	z	Distance of ply mid-plane from laminate mid-plane
ϵ_x	Buckling strain		
λ	Half-wavelength in x axis in VIPASA	$(\text{EA})_{\text{bay}}$	Axial stiffness of a single stiffener bay
ξ_1^A, ξ_2^A	In-plane lamination parameters	$(\text{EA})_{\text{st}}$	Axial stiffness of additional stiffener section
ξ_1^D, ξ_2^D	Out-of-plane lamination parameters	$\mathbf{A}$	In-plane stiffness matrix
b_{ext}	Extension of 'Outer' width	$\mathbf{B}$	In-plane/out-of-plane coupled stiffness matrix
b_{fl}	Stiffener flange width	$\mathbf{D}$	Out-of-plane stiffness matrix
b_{seam}	Seam width	$\mathbf{U}$	Material invariants vector
b_{st}	Stiffener bay spacing length	L	Panel length
F_i	Buckling factors	P_x	Overall applied load

*Corresponding author

1. Introduction

Fibre-reinforced composite materials are employed widely in the aerospace industry due to their superior specific stiffness and strength properties. Composites are also attractive due to an ability to tailor fibre orientations to suit given design requirements. Current industrial practice, however, does not make use of the full potential of this tailoring, as panels typically employ a constant stiffness design, where the ply orientations and laminate thickness are constant throughout a structure. Variable stiffness designs, in which fibre angle is varied across a single ply, have consequently gained recent interest.

Variable stiffness designs redistribute in-plane loads within a structure leading to theoretical improvements in buckling and post-buckling behaviour of flat panels [1–3], and increased strength in laminates with circular holes [4, 5] compared to constant stiffness designs. Spatial variation of a single ply angle can be achieved continuously or in a piecewise manner, i.e a 'patch' design, within a part. Continuous fibre steering, where the fibre path is varied continuously across the width, is a typical manufacturing method for the creation of variable stiffness parts [6], however, practical designs are still significantly limited by process imposed constraints, speed of manufacture or unacceptable defects [7]. For example, Automated Fibre Placement can result in ply gaps, overlaps and fibre kinking [6]. These disadvantages prompted the creation of the Continuous Tow Shearing process, which utilises shearing tows to produce continuous curvature [8]. Both methods suffer from the imposition of a minimum manufacturable turning radius for a steered ply, restricting the maximum performance benefit achievable [9, 10].

An alternative tailoring method, Discrete Stiffness Tailoring (DST), alters the ply angle using discrete strips across the width of a structure, allowing for greater flexibility in the design of variable stiffness structures. This method benefits from being compatible with high-deposition automated manufacturing techniques such as Automated Tape Laying (ATL), which is able to accomplish both a high rate and precise deposition of unidirectional prepreg suitable for these designs [11]. Discrete Stiffness Tailoring has shown both experimentally and analytically to increase flat panel buckling stresses for a given weight [12, 13] at the cost of introducing fibre discontinuities within a structure (seams) which may be susceptible to failure. However, an initial exploratory experimental study in [13] found no damage within seams placed parallel to the applied load in experimental buckling panels and complimentary tensile seam tests determined that significant strength is preserved even if a majority of plies contain discrete changes in ply orientation.

The optimum design of composite structures is intrinsically challenging owing to: non-linearity and non-convexity of the design space, large numbers of both discrete ply stacking, continuous fibre orientation and geometric variables. Optimisation of variable stiffness laminates poses even greater difficulty as the variability of ply angles and laminate thicknesses across the structure must be considered alongside the enforcement of blending or constraining the permissible steering radius [14]. Compared with the general continuous case, parametrising the fibre angle path to vary curvilinearly reduces the number of variables and maintains continuity across the width of a structure [15–18]. However, these path functions must be redefined for alternative geometries and so do not provide a general optimisation framework. Formulating the problem as a discrete patch methodology provides greater design flexibility

but more constraints are necessary to enforce compatibility and ply continuity between regions [19, 20].

Optimisation using non-dimensional lamination parameters can overcome the limitations associated with ply angles [21, 22] and requires a maximum of twelve lamination parameters, reducing to four parameters to describe the stiffness of any specially orthotropic laminate and can be applied to stiffness and buckling optimisation problems [23, 24]. Laminate stiffness has linear dependence upon lamination parameters leading to convex optimisation problems [25]. Optimisation with lamination parameters to create a discrete stacking sequence requires a two-level optimisation methodology, the first stage using continuous lamination parameters and the second stage returning discrete stacking sequences to match these optimum lamination parameters. This section stage is often undertaken using a Genetic Algorithm (GA) [26–30] which can handle the problem of combinatorial discrete variables, and penalty functions are also easily employed to enforce manufacturing constraints [31]. Wu et al. [32] extended this to the optimisation of Variable Angle Tow (VAT) composite plates with curvilinear fibres, ensuring strict enforcement of feasibility constraints at all spatial coordinates during optimisation by parametrising lamination parameters using Non-Uniform Rational B-Splines (NURBS). This optimisation methodology has been shown to be computationally efficient and robust, and can be used as a generic solution for a variety of problems. NURBS parametrisation of the fibre angle can also be easily coupled with accurate yet efficient isogeometric analysis for the buckling load optimisation of variable-stiffness panels [33, 34]. An interpolation method [35] that controls the magnitude and direction of change of lamination parameters across a VS structure can also be employed to generate smooth manufacturable fibre paths, whilst retaining the benefits of lamination parameter based optimisation. Analytical models are often used in optimisation studies as these can be solved more efficiently than Finite Element (FE) analyses. The derivation of closed-form equations based upon a Rayleigh-Ritz approach is particularly common [16, 27, 36, 37] and the results from these show excellent correlation with FE models. Coburn et al. extended the Rayleigh Ritz approach in [16] to the buckling analysis of a VAT stiffened panel, and this model could potentially be used in an efficient optimisation strategy [38]. An alternative approach is the use of a finite strip model, which solves the governing equations exactly for prismatic structures discretised into lengthwise strips [39, 40].

A maturity assessment of the variable stiffness design methods conducted by Sabido et al. [41] found that although the performance improvements of simple panels with stiffness tailoring can be well-predicted and are validated with limited experimental tests [42–44], there is a lack of work quantifying the benefit of applying this to complex structural components. Some structural level variable stiffness aerospace parts have been created: a wingbox with a fully steered skin was designed, manufactured and tested by Oliveri et al., but this was not optimised [45]. A third-scale minimum-mass wingbox was optimised for both aerodynamic and structural constraints, then manufactured and tested [46], however, the fibre stacking sequence is restricted to be locally orthotropic with respect to the global tow path, and these stacks are created of plies with predefined curved fibre architectures. The pre-set curved fibre geometry and stacking sequence reduces the number of variables but overly constrains the design space.

In this paper, the Discrete Stiffness Tailoring methodology is extended from the work in [13] to the optimisation of a realistic engineering structure. A stiffened panel is selected as an example of such a structure, as these panels are commonly used to carry compressive loads in aircraft components and have buckling as a critical mode of

failure [47]. The widely-used two-stage lamination parameter-based optimisation methodology is adapted to achieve optimum design of structures comprised of discretely tailored strips. The developed method is demonstrated by minimum-mass optimisation of a stiffened panel under compressive load, subject to buckling and longitudinal strain constraints. The resulting design is manufactured and experimentally tested in order to validate this novel tailoring framework. The primary contribution of this paper is the demonstration of this design and manufacturing philosophy at an assembly level for the first time, to achieve large-scale variable stiffness panels uninhibited by restrictions on fibre deposition radii.

In Section 2, the stiffened panel geometry and the application of DST to the panel skin are described. Section 3 covers Classical Laminate Theory and lamination parameter expressions, and Section 4 details the two-stage optimisation methodology. A numerical study, comparing baseline and DST designs is presented in Section 5. Section 6 explains the manufacturing and experimental procedure for the DST panel, Section 7 summarises FE analysis of the DST panel, and Section 8 presents experimental and numerical results, and discusses these. Final conclusions are presented in Section 9.

2. Discrete Stiffness Tailoring Philosophy

A T-stiffened panel of length L, illustrated in Figure 1, is selected as a suitable representative aircraft structure for the demonstration of DST. The panel is assumed to be an upper wing cover carrying a compressive uni-axial load N_x; the loading edges are assumed clamped, whilst the longitudinal edges are free of restraint. This longitudinal boundary condition is not typical of aerospace structures which are approximately simply-supported, but this is selected to be compatible with test machine constraints. A two-stiffener design was selected for experimental feasibility, such that sufficient skin-width is present for optimisation while ensuring the panel may be manufactured and tested within the available test machine. The panel is composed of a single skin and two T-shaped stiffeners that are attached at either longitudinal edge, separated by a stiffener spacing length. The critical buckling load is assessed as the main design constraint and a maximum strain allowable is also enforced for damage tolerant design, as this imposes a minimum value on overall panel stiffness.

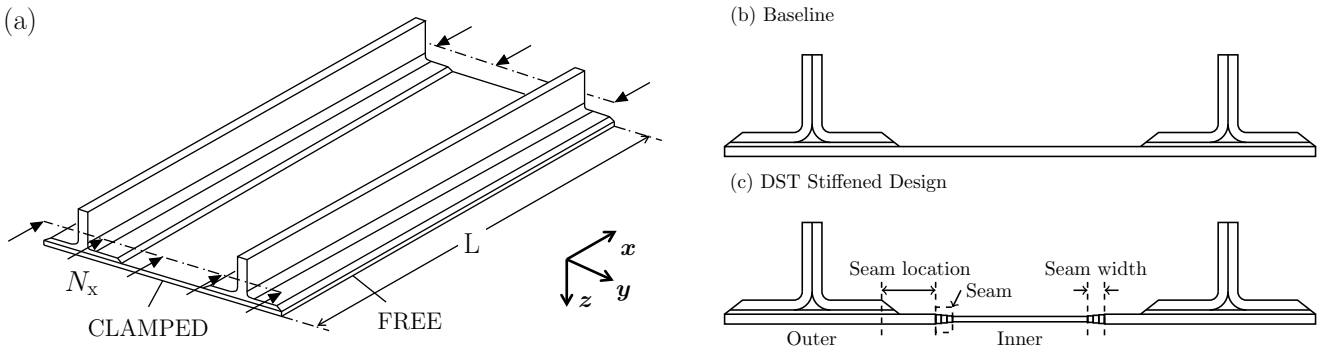

Figure 1: a) Isometric view of the panel, length L, indicating boundary conditions and loading N_x applied as uniform end-shortening. Cross-sections of b) baseline case, and c) Discrete Stiffness Tailored panel, the 'Outer' and 'Inner' skin regions are linked by 3 segment stepped seam, and the seam location is measured as the distance from the stiffener foot.

Tailoring is applied across the skin by division into two regions: underneath the stiffener bond-line - the 'Outer' region, and the length of skin between the stiffeners - the 'Inner' region as labelled on the panel cross-section in Fig. 1c. Transition between the two skin regions is established by way of three piecewise steps (the seam region) which individually have constant thickness and stiffness but in which the thickness and stacking sequence is varied in discrete steps in order to avoid large stress concentrations and formation of damage in the weaker resin rich region due to discrete ply drops. The 'Outer' region width extends beyond the stiffener foot and the model is able to optimise the location of the transition. With curvilinear variable angle designs the size and site of the transition region is generally dictated by the minimum manufacturable radii, whereas transition can occur as rapidly as needed with the new DST design methodology presented here. The aim of the DST design is to redistribute the load by providing reinforcement where required in the structure, leading to a more efficient use of material which in turn results in a reduction in mass. It should be noted that the stiffened panel optimisation problem investigated here is different to those papers, e.g. [1–3], in which edges of flat plates are artificially stiffened by external fixturing which is then exploited in the design optimisation process. Here, instead, the stiffened panel incorporates stiffening that is intrinsic to its design as the stiffness, dimensions and mass of the stiffeners are directly affect the value of objective function of the optimisation procedure i.e. the mass of the overall panel.

3. Classical Laminate Analysis & Lamination Parameters

Classical Laminate Theory (CLT) is widely used to define the elastic properties of a laminate stack [22]. The in-plane, coupled response and out-of-plane (**ABD**) stiffness matrices are related to the applied moments and stresses, and the resultant mid-plane strains and curvatures, as follows:

$$\begin{Bmatrix} \boldsymbol{M} \\ \boldsymbol{N} \end{Bmatrix} = \begin{Bmatrix} \mathbf{A} & \mathbf{B} \\ \mathbf{B} & \mathbf{D} \end{Bmatrix} \begin{Bmatrix} \boldsymbol{\epsilon}^0 \\ \boldsymbol{\kappa} \end{Bmatrix} \tag{1}$$

Using lamination parameters, any full laminate stack may be described using a single thickness variable, t, five material invariants, $\boldsymbol{U}$ and twelve lamination parameters, regardless of the number of plies [21]. The twelve lamination parameters can be further reduced to eight for symmetric laminates, as the coupled response matrix $\mathbf{B}$ becomes zero. For balanced laminates, extension shear coupling terms (A_{16}, A_{26}) are exactly zero, whereas bend-twist coupling terms (D_{16}, D_{26}) can be made close to zero through the ordering of the plies within a stack. Such behaviour is targeted by the optimisation routine in this paper, and as such the lamination parameter terms relating to extension-shear ($\xi^A_{3,4}$) or bend-twist coupling ($\xi^D_{3,4}$) are assumed to be zero in the Stage I analysis, although this is not always achieved in the discrete stacking sequences obtained in Stage II. The expressions that relate the $\mathbf{A}$ and $\mathbf{D}$ matrices to these lamination parameters are therefore simplified to the following:

$$\begin{pmatrix} A_{11} \\ A_{22} \\ A_{12} \\ A_{66} \end{pmatrix} = t \begin{bmatrix} 1 & \xi^A_1 & \xi^A_2 & 0 & 0 \\ 1 & -\xi^A_1 & \xi^A_2 & 0 & 0 \\ 0 & 0 & -\xi^A_2 & 1 & 0 \\ 0 & 0 & -\xi^A_2 & 0 & 1 \end{bmatrix} \begin{pmatrix} U_1 \\ U_2 \\ U_3 \\ U_4 \\ U_5 \end{pmatrix} \tag{2}$$

$$\begin{pmatrix} D_{11} \\ D_{22} \\ D_{12} \\ D_{66} \end{pmatrix} = \frac{t^3}{12} \begin{bmatrix} 1 & \xi_1^D & \xi_2^D & 0 & 0 \\ 1 & -\xi_1^D & \xi_2^D & 0 & 0 \\ 0 & 0 & -\xi_2^D & 1 & 0 \\ 0 & 0 & -\xi_2^D & 0 & 1 \end{bmatrix} \begin{pmatrix} U_1 \\ U_2 \\ U_3 \\ U_4 \\ U_5 \end{pmatrix} \tag{3}$$

where the four lamination parameters are given by:

$$\xi_{1,2}^A = \frac{1}{t} \int_{-t/2}^{t/2} [\ cos(2\theta),\ cos(4\theta)\ ] dz \tag{4}$$

$$\xi_{1,2}^D = \frac{12}{t^3} \int_{-t/2}^{t/2} [\ cos(2\theta),\ cos(4\theta)\ ] z^2\ dz \tag{5}$$

and z is the distance of mid-plane of the ply from the mid-plane of the laminate which has overall thickness t, and θ is an individual ply angle.

4. Optimisation Methodology

A two stage optimisation routine is employed, as per those developed in [26, 27], as detailed in Figure 2. The first stage returns optimal lamination parameters, structural thicknesses and relative widths for the panel, using a gradient-based optimisation method. This initial optimisation is performed in MATLAB, using the non-linear programming function 'fmincon'. The second stage utilises a genetic algorithm to minimise the difference between the optimal continuous lamination parameter design and a candidate discrete stack, as no one-to-one mapping exists for the inverse transformation. A summary of the objective, constraints and decision variables associated with each optimisation stage is provided in the subsequent sections.

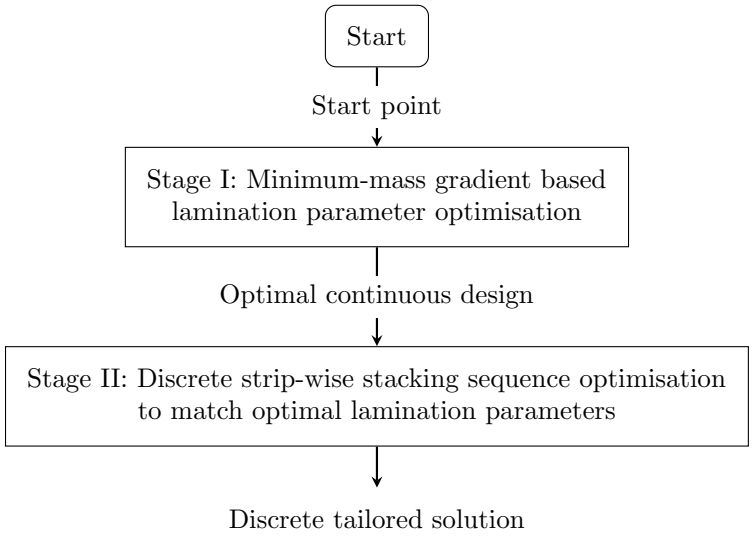

Figure 2: Flowchart of optimisation process stages.

4.1. Stage I: Gradient based lamination parameter optimisation

4.1.1. Objective

The objective function is the mass of a single stiffener bay, calculated from the geometric variables. Various linear and non-linear inequality constraints are applied which govern structural performance, manufacturing rules, and lamination parameter feasibility. The optimisation problem, where $\boldsymbol{x}$ is the vector of design variables, is therefore formulated as follows:

$$\begin{aligned} &\text{minimise } f(\boldsymbol{x}) \\ &\text{subject to } g(\boldsymbol{x}) \leq 0 \\ &\text{and } \boldsymbol{x}_{lb} \leq \boldsymbol{x} \leq \boldsymbol{x}_{ub} \end{aligned} \tag{6}$$

where $f(\boldsymbol{x})$ is the objective function, which is the mass as previously described, $g(\boldsymbol{x})$ are the constraints, and $\boldsymbol{x}_{lb}$ and $\boldsymbol{x}_{ub}$ are vectors describing the lower and upper bounds respectively for the corresponding design variables, $\boldsymbol{x}$. Each of the components of Eq. 6 are described in detail in the subsequent sections.

4.1.2. Variables

All variables are normalised to lie on the unit interval for improved solver performance. Lamination parameters ($\xi_{1,2}^{A,D}$) are employed as Stage I variables, describing the stiffness properties of each discrete region of the panel. Lamination parameters and thicknesses in the seam region are taken as discrete values from a linear trend varying between their corresponding values in the 'Outer' and 'Inner' regions, evaluated at each seam mid-line. The geometric variables to be optimised for each panel type are listed in Table 1 and are indicated on the cross-section of the DST panel in Fig. 3. Other labelled variables in Fig. 3 are submitted to the optimiser as fixed values; including the outer stiffener radius r_{st}, the seam width b_{seam}. As is standard industrial practice, two plies of $\pm 45°$, spanning the width of both stiffener flanges and referred to as 'capping plies', are included to contain the noodle within the deltoid region of the stiffener.

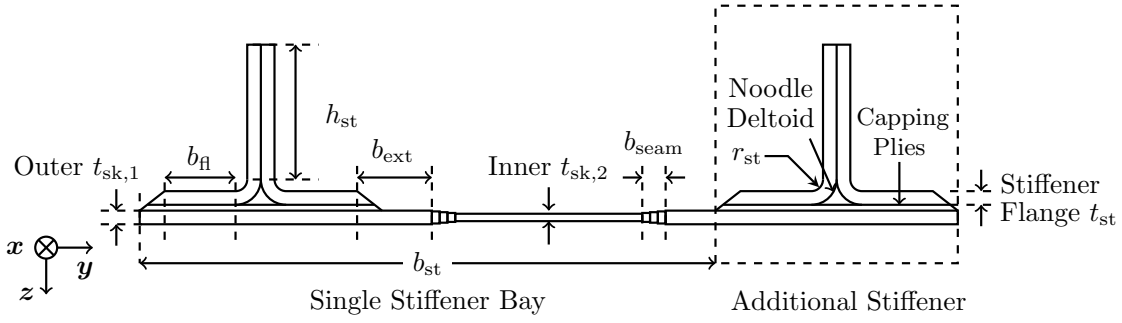

Figure 3: Cross-section of the DST panel labelled with geometric variables.

Panel Type	Skin	Stiffener
Baseline	$(\xi_{1,2}^{A,D})_{\mathrm{sk}}$, t_{sk}	t_{st}, h_{st}, b_{fl}
DST	Outer $(\xi_{1,2}^{A,D})_{\mathrm{sk},1}$, $t_{\mathrm{sk},1}$, b_{ext}	t_{st}, h_{st}, b_{fl}
	Inner $(\xi_{1,2}^{A,D})_{\mathrm{sk},2}$, $t_{\mathrm{sk},2}$	

Table 1: Stage I: Table of design variables

4.1.3. Applied Load

The design running load N_x is prescribed as a compressive force per unit width, homogenised across a single stiffener bay. The total load applied to the panel must therefore be adjusted to account for the fact that two stiffeners are modelled. Specifically, variations in the axial stiffness of the additional stiffener and the attached skin section, resulting from changes in the design variables, will attract varying levels of running load into the panel. The overall applied load P_x is calculated by adding an additional contribution to the load associated with the additional stiffener section $(\mathrm{EA})_{\mathrm{st}}$ proportional to the axial stiffness of a single stiffener section divided by that of a complete stiffener bay $(\mathrm{EA})_{\mathrm{bay}}$, these regions are marked on Fig. 3. For a structure composed of N plates, the axial stiffness is expressed as:

$$(\mathrm{EA})_i = \sum_{i=1}^{N} b_i \left(A_{11,i} - \frac{A_{12,i}^2}{A_{22,i}} \right) \tag{7}$$

where subscript i refers to the strip number in VIPASA, see Section 4.1.4.

Obtaining both $(\mathrm{EA})_{\mathrm{st}}$ and $(\mathrm{EA})_{\mathrm{bay}}$, the overall applied load is calculated as:

$$\mathrm{P}_x = N_x \, b_{\mathrm{st}} \left(1 + \frac{(\mathrm{EA})_{\mathrm{st}}}{(\mathrm{EA})_{\mathrm{bay}}} \right) \tag{8}$$

4.1.4. Buckling Constraints

Buckling constraints are applied to prevent the stiffener or skin buckling prematurely before the design load is reached. A finite strip program, VIPASA [48], is used to predict the buckling behaviour of the panel. Buckling modes are assumed to vary sinusoidally in the longitudinal direction x in Fig. 1a with half-wavelength λ, the number of modes, N, are specified by the user and the half-wavelengths values are taken as $\lambda = \ell$, $\ell/2$, ..., ℓ/N where $\ell = \mathrm{L}/2$ is the effective length of the panel. As a result of this assumption, the displacements, rotations and, correspondingly, the forces and moments at the longitudinal edge also vary sinusoidally. In the absence of shear load or bend-twist coupling VIPASA modeshapes correspond to simply-supported transverse boundary conditions. In order to obtain buckling results for the stiffened panel structure with clamped end boundary conditions as indicated in Fig. 1, the VIPASA model has a length of half the actual panel length, as the effective length factor for a column with both ends fixed is equivalent to half that of a column with both ends pinned.

The exact stiffness matrices for an individual plate are explicitly obtained as a function of the edge forces and displacements using classical plate theory [49]. The subsequent transcendental eigenproblem is solved using the

iterative Wittrick-Williams algorithm [50], an efficient modelling approach which guarantees convergence on all specified eigenvalues. The analysis returns a list of eigenvalues, the buckling loads and a modeshape plot associated with each i^{th} half-wavelength specified. A sufficiently large range of half-wavelengths is assessed in this analysis to encompass critical global, local skin and local stiffener buckling modes. Buckling factors F_i are calculated by dividing these eigenvalues by the applied in-plane loading. Hence a buckling constraint is evaluated as follows:

$$1 - F_i \leq 0 \tag{9}$$

4.1.5. Strain Constraint

The axial strain of the entire structure is limited to an allowable value, $\epsilon_{\max}$. The smeared panel axial stiffness is calculated using Eq. (7) which models the regions as connected parallel springs, dividing by the width of the panel, and the strain ϵ_x is returned using Eq. (1). The strain constraint is then evaluated using the design strain $\epsilon_{\max}$ as follows:

$$\frac{\epsilon_x}{\epsilon_{\max}} - 1 \leq 0 \tag{10}$$

4.1.6. Lamination Parameter Feasible Regions

Lamination parameters are interdependent variables. No bijective function exists between any combination of in-plane, in-and-out-of-plane or out-of-plane parameters, so for a given point in the $\xi^A_{1,2}$ space, there exists a number of possibilities for the selection of $\xi^D_{1,2}$, and vice-versa. A number of non-linear constraints define the outer limit for the selection of lamination parameters and also the relationships between the in-plane, coupling and out-of-plane regions. Some manufacturing constraints can also be accounted for at this stage. For symmetric laminates composed of standard angles (0°, ±45°, 90°), the constraint relating the in-plane and out-of-plane parameters are as follows [24]:

$$2\,|\,\xi^j_1| - \xi^j_2 - 1 \leq 0 \qquad j = A, D \tag{11}$$

Additional constraints that link the in-plane and out-of-plane lamination parameters for standard angle laminates are derived in [51]. These constraints form conceptually similar boundaries to the feasible region illustrated in Fig. 4, however, spanning the full nine-dimensional space of in-plane and out-of-plane, and coupling lamination parameters corresponding to standard angle laminates. Herencia et al. then accounted for symmetric laminates, defining 10 constraints which are fully derived in [52]. Setting $\xi^{A,D}_3$=0, and eliminating constraints which are never active gives rise to the following 8 constraints:

$$(\xi^A_i - 1)^4 - 4(\xi^A_i - 1)(\xi^D_i - 1) \leq 0 \qquad i = 1, 2 \tag{12a}$$

$$(\xi^A_i + 1)^4 - 4(\xi^A_i + 1)(\xi^D_i + 1) \leq 0 \qquad i = 1, 2 \tag{12b}$$

$$(2\xi^A_1 - \xi^A_2 - 1)^4 - 16(2\xi^D_1 - \xi^D_2 - 1)(2\xi^A_1 - \xi^A_2 - 1) \leq 0 \tag{12c}$$

$$(2\xi^A_1 + \xi^A_2 + 1)^4 - 16(2\xi^D_1 + \xi^D_2 + 1)(2\xi^A_1 + \xi^A_2 + 1) \leq 0 \tag{12d}$$

$$(2\xi^A_1 - \xi^A_2 - 3)^4 - 16(2\xi^D_1 - \xi^D_2 - 3)(2\xi^A_1 - \xi^A_2 - 3) \leq 0 \tag{12e}$$

$$(2\xi^A_1 + \xi^A_2 + 3)^4 - 16(2\xi^D_1 + \xi^D_2 + 3)(2\xi^A_1 + \xi^A_2 + 3) \leq 0 \tag{12f}$$

4.1.7. Lamination Parameter Manufacturing Constraints

In order to account for unanticipated off-axis loading, it is common industrial practice to maintain a 10% minimum of the overall laminate thickness of each standard angle ply (0°, ±45°, 90°). This common practice reduces the feasible regions in the in-plane and out-of-plane lamination parameter space as illustrated in Fig. 4. The limits of the constrained out-of-plane region are defined by 6 points, each representing the extreme stacking sequence combinations of 0°/±45°/90° plies, as described by Liu [53], however, a triangular feasible region can be approximated for simplicity. For the in-plane parameters, the space is considerably reduced due to the 10% rule, but little reduction is observed in the out-of-plane feasible region. A more detailed discussion of the application of the 10% rule for lamination parameter optimisation can be found in [54], in which the rule is extended to cover non-standard angles, as well as the traditional set.

As all variables are transformed onto the unit interval, the application of upper and lower bounds to the lamination parameter variables scales the entire region to now lie between these bounds, given in Table 2. In doing this, all feasible regions constraints defined in Eqs. (11-12) are automatically scaled to fall within these bounds, including those linking the in-plane and out-of-plane parameters.

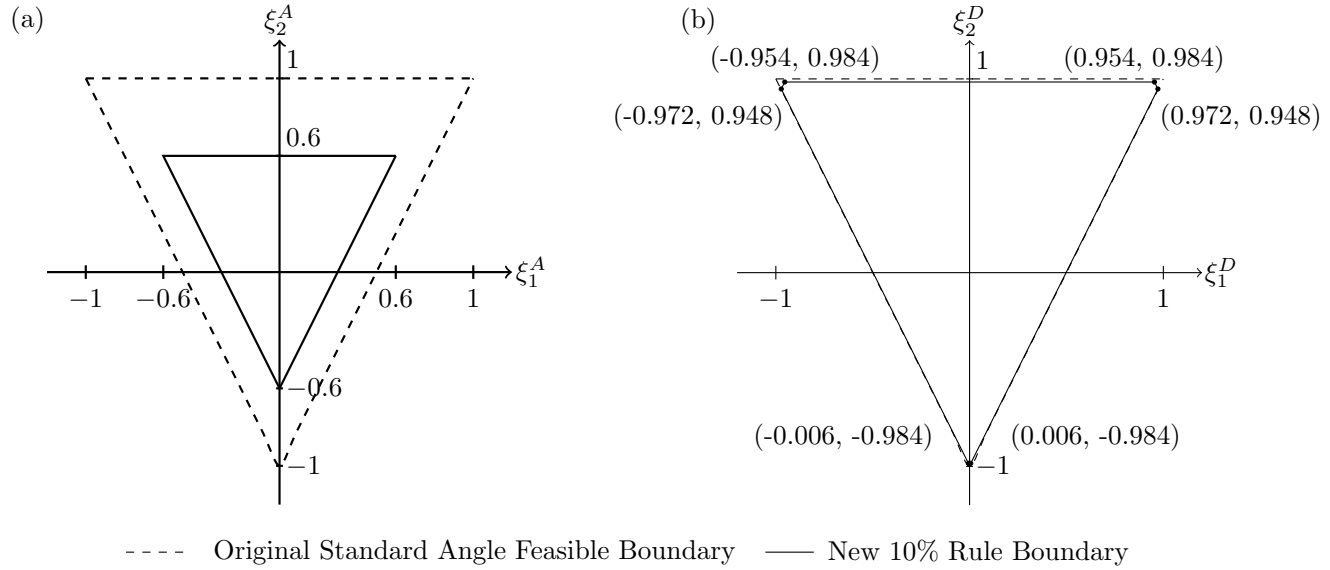

Figure 4: Reduced feasible region for the (a) in-plane (membrane) and (b) out-of-plane (flexural) lamination parameters considering the use of only standard angles (0°,±45°, 90°) and imposing the 10% rule. The original boundary, denoted by dotted lines, is given for comparison.

	ξ_1^A	ξ_2^A	ξ_1^D	ξ_2^D
Lower Bound	-0.6	-0.6	-0.972	-0.984
Upper Bound	0.6	0.6	0.972	0.984

Table 2: Lamination parameter upper and lower bounds.

4.1.8. Geometric Constraints

A linear constraint is enforced to ensure the stiffener spacing remains fixed to value b_{st}, under variations in the flange length and extension of the skin outer regions beyond the stiffener flange. Another linear constraint ensures the difference in thickness between the outer and inner skin regions across the seam width distance b_{seam} is not too large. This constraint is based upon current industrial guidelines which enforce a ratio of 10:1 between transition width and thickness variation in components where the taper is transverse to the loading direction [55]. This linear constraint is defined as:

$$|t_{\text{sk},1} - t_{\text{sk},2}| \leq \frac{b_{\text{seam}}}{10} \tag{13}$$

4.2. Stage II: Stacking Sequence Design

In Stage II of the optimisation, a Genetic Algorithm is used to find stacking sequences that best match the continuous optimal thickness and lamination parameters. In order to satisfy the performance constraints, the ply thicknesses are rounded up to to result in an integer number of plies, n_{ply}. The 'Outer' and 'Inner' stacking sequences are returned by separate GA runs, with no constraint to match with the stacking sequence in one region with that in the other. In Stage I, the lamination parameters and thicknesses of the stepped seam are assumed to be linear variations between those of the 'Outer' and 'Inner' regions. In Stage II, the seam stacking sequences are obtained by targeting a linear variation in the returned ply stacking sequence percentages for the 'Inner' and 'Outer' regions, with some manual adjustment to ensure a smooth and blended transition, maintaining continuous plies across the width where possible.

4.2.1. Objective

The objective function is to minimise the euclidean distance between the target lamination parameters (ξ_{opt}) and the calculated lamination parameters (ξ_{ga}) for the candidate stacking sequence, which is expressed following the example of Diaconu and Sekine [51]:

$$f(\boldsymbol{x}) = \sum_{i=1}^{4} w_i^A \, (\, \xi_{i,ga}^A - \xi_{i,opt}^A)^2 + \sum_{i=1}^{4} w_i^D \, (\, \xi_{i,ga}^D - \xi_{i,opt}^D)^2 \tag{14}$$

where $\boldsymbol{x}$ is a vector of design variables representing the ply orientations.

All eight in-plane and out-of-plane lamination parameters $\xi_{1-4}^{A,D}$, where $\xi_{3,4}^{A,D} = 0$ consistent with Stage I assumptions, are used in the calculation of the objective function to ensure extension-shear and bend-twist coupling characteristics are minimised. Weighting parameters (w^A, w^D) can be applied to prejudice the optimiser to better

match specific lamination parameters than others. In this case, the in-plane parameters were targeted to a greater extent than the out-of-plane component of the stiffness variables. Two penalty terms, $g_{10\%}(\boldsymbol{x})$ and $g_{\text{contiguity}}(\boldsymbol{x})$, are added to the fitness function to account for the 10% rule and ply contiguity constraints.

4.2.2. 10% Rule Constraint

The 10% rule has previously been enforced through the restriction of the lamination parameter feasible region. In general, this ensures that the genetic algorithm generated stacking sequences do not violate this rule. For thin laminates it is well known that matching lamination parameters with a small amount of discrete plies is difficult [28]. To ensure that the 10% rule, initially enforced in Stage I, is not subsequently violated to achieve a better match, a penalty function is applied in Stage II to maintain at least a 10% proportional of each ply angle. This function is expressed as:

$$g_{10\%}(\boldsymbol{x}) = \sum_{j=1}^{4} \Pi_j \begin{cases} \Pi_j = 1, & \text{when } n_j < 0.1\, n_{\text{ply}} \\ \Pi_j = 0, & \text{otherwise} \end{cases} \tag{15}$$

where n_j is the total number of plies with the j^{th} orientation and Π_j .

4.2.3. Stacking Sequence Rules

The following rules are applied to the stacking sequence design for the stiffened panel. Some are taken from Niu [47], and they have been supplemented with additional considerations due to the discrete tailoring across the width:

(i) Laminates are balanced and symmetrically stacked about the midplane, to prevent both warping of the laminate during cure and coupling of in-plane and out-of-plane elastic response.

(ii) $\pm 45^\circ$ plies are positioned on the outer surface of the laminate for increased damage tolerance.

(iii) A maximum 4-ply contiguity is enforced to prevent high transverse stress gradients in the laminate and to avoid delaminations.

(iv) Plies on the bondline between skin and stiffener are of the same orientation, and not in the principal direction (i.e. 0°) to ensure load is transferred through shear.

Symmetry is enforced by optimising half the stack, with the remaining plies mirroring these variables about the mid-plane. The outer plies are pre-assigned to $\pm 45^\circ$ to satisfy constraints (ii) and (iv). A penalty function is employed to enforce the ply contiguity constraint as per [52, 56]:

$$g_{\text{contiguity}}(\boldsymbol{x}) = \Theta \tag{16}$$

where Θ is the total number of instances within the stacking sequence where more than four plies of the same orientation are stacked contiguously.

5. Numerical Study

The presented optimisation methodology is applied to two cases: a baseline constant skin thickness panel and a DST stiffened panel as illustrated in Fig. 1. In order to evaluate the optimisation methodology, the DST panel was manufactured and tested, which required some additional manufacturing constraints to be implemented for the numerical study. The panels are designed using AS4-8552 CFRP, with the material properties E_{11}= 114.3 GPa (compressive modulus), E_{22}= 8.8 GPa, G_{12}= 4.9 GPa, ν_{12}= 0.314, ρ= 1580 kg/m^3, and a ply thickness of 0.196 mm [57].

The first stage of the optimisation routine is applied to the panels defined using the fixed parameters in Table 3. The design compressive load per unit width of N_x = 1 kN/mm is selected to represent the loading experienced midway between the tip and root of a wing on a standard narrow bodied aircraft and the strain constraint is set at 4500 µstrain based on industrial limits for damage tolerance. Both the baseline and tailored panel use a fixed stiffener spacing (b_{st}) of 300 mm, and the industrial standard angle stacking sequence percentage ratio, 60%/30%/10% for 0°/45°/90° respectively [40], predetermines the elastic properties of the stiffeners for Stage I.

For the tailored panel, the seam region width (b_{seam}) is fixed at 30 mm, this is selected to be arbitrarily large as the transfer of load due to shear stress requires a comparably small overlap. The geometric variables are bounded between values deemed appropriate for the design problem in question, as given in Table 4, and lamination parameter bounds are as detailed in Table 2. The lower bound for the stiffener flange, b_{fl}, is chosen as 35 mm which is the minimum length that allows for bolted repairs. For both panels, the material within the stiffener deltoid region, indicated in Fig. 3, is not modelled to contribute structurally to the buckling behaviour of the panels in the optimisation routine.

Parameter	Value
N_x (kN/mm)	1
$\epsilon_{\max}$ (µstrain)	4500
b_{st} (mm)	300
b_{seam} (mm)	30
r_{st} (mm)	5
Panel length, L (mm)	1000

Table 3: Fixed parameters: Numerical study

	t	h_{st}	b_{fl}	b_{ext}
	(mm)			
Lower Bound	2	5	35	1
Upper Bound	10	60	70	100

Table 4: Variable upper and lower geometric bounds; t refers to bounds applied to each thickness variable.

Matched stiffener tooling is only available for radii with an integer number of millimetres, and as such it is necessary to round the Stage I returned stiffener thickness to the nearest millimetre to facilitate manufacturing of the designs. A stacking sequence is obtained with this updated stiffener thickness using Stage II as outlined in Section 4.2. The model is subsequently updated to reflect the new stiffener thickness and stacking sequence design, and the Stage I gradient-based optimisation is undertaken again. All runs of the Stage II GA use a population of 40, 200 generations, a crossover probability of 0.7, and each generation retains 6 elite candidates. Weighting for the lamination parameters is selected to give greater importance to the in-plane parameters; $w_i^A = 1.5$ and $w_i^D = 1$. For the DST case, the 'Outer' and 'Inner' stack matching problems are submitted to the GA separately. As

in Stage I, a linear stiffness variation is assumed to describe the transition over seam regions, and the 'Inner' and 'Outer' stacking sequences are blended manually to reflect this linear stiffness change.

5.1. Optimisation Results

The optimum designs obtained at each stage of the optimisation routine are presented in Table 5, and the final discrete stacking sequence designs and panel masses are detailed in Table 6. A convergence plot for both designs in Stage I is shown in Fig 5. The reduction in mass for a single stiffener bay, achieved by comparing the final discrete laminate design to the optimised baseline case, is 14.4%. Reasonable agreement between the lamination parameters obtained at the first and second stages was generally achieved, see Table 5, with the exception of the in-plane parameters for the baseline stiffener design, as the small discrete number of plies in this case limit the procurement of a suitable matching candidate. Bend-twist coupling is present in the final discrete designs, but these are very small compared to the other laminate stiffness terms. To achieve a blended design between the 'Inner' and 'Outer' skin region, a linear variation in the standard angle ply percentages and thicknesses was assumed. In order to allow a more gradual transition of total laminate stiffness and thickness, unbalanced laminate configurations were permitted for Seam 2 and 3, listed in Table 6.

Cross-sections of the baseline and DST final panel designs are illustrated in Fig. 6 which shows the significant difference in the distribution of mass and stiffness between each panel. The discrete stiffness tailoring redirects the stiffness, and therefore load, in the panel through the stiffener and the 'Outer' skin region, which is composed of the largest possible proportion of 0° plies allowed by the 10% rule. The 'Inner' skin region conversely is created of the maximum proportion of ±45° plies with little laminate thickness, as needed only for buckling resistance in the free skin region. In contrast, the optimum baseline skin design ply percentages are typical of the aerospace industrial skin ratio of 44%/44%/12% which bear the significant majority of the compressive load, while the stiffener contributes a small amount of stiffness to the panel, but significant resistance to a global mode due to an increased second moment of area. The 10% rule indirectly maintains some fully continuous plies across the width of the skin panel that provide some seam strength, despite inhibiting the feasible lamination parameter space for the DST skin design.

The achievable mass reduction for both the baseline and DST panel types is limited by the lower bound for bolted repairs as the 35 mm minimum is reached at all stages of the optimisation routine, the results of which are given in Tables 5 & 6. For the DST design, the constraint which limits the difference in thickness between the 'Inner' and 'Outer' regions was active in the DST design, which suggests that a more significant mass saving could be achieved if there was some relaxation of the industrial taper constraints. The extension of the 'Outer' skin beyond the stiffener flange (b_{ext}) also returned the lower bound, resulting in an immediate transition beyond the edge of the stiffener foot, illustrated in Fig 6b. This result suggests that a rapid transition from the outer to inner skin design is ideal which is a distinct advantage of the discrete tailoring technique over continuous fibre steering.

The VIPASA buckling analysis is performed for N = 30 modes, taking half-wavelength lengths of $\lambda = \ell$, $\ell/2$, ..., $\ell/30$, where $\ell = \text{L}/2$ is the effective panel length. The resulting modeshape plots for each half-wavelength are returned, indicating if the mode occurs locally in the skin or stiffener web, or globally, alongside the buckling load

factors for each case. The buckling factors, applied load and critical buckling strain for the designs are presented in Table 7. A local skin buckle is the critical buckling mode for both the baseline and DST optimised panel designs. Reviewing the modeshape plots for the specified half-wavelengths the DST case exhibits both global and skin buckling, whereas the baseline case buckles in skin and stiffener local modes. The baseline panel is too stiff and its second moment of area too large to result in global buckling at the given panel length, and the stiffener buckling occurs at 150% of the design load, exhibiting a large amount of redundancy and excess mass in the baseline design. In contrast, the reserve for the global and skin modes in the DST case are both close to one, and stiffener buckling is made impossible by the stiffener thickness and stubby web height of the DST design. By tailoring the skin to increase the buckling capacity of the panel, the stiffener height can be greatly reduced as the contribution of the web to the second moment of area is no longer needed. With the application of DST, stiffener sizes can be potentially reduced, alongside a possible increase in the stiffener spacing. The unsupported longitudinal boundary conditions do not represent realistic wing panel applications, which are much wider, with many more stiffeners, and longitudinal supports at spars. However, restraining the longitudinal edges from out-of-plane deformation to produce a simply-supported boundary condition would increase the global buckling factor. As the critical buckling modes for both baseline and DST panels include such overall modes, as well as skin modes which are generally unaffected by the longitudinal supports, it would be anticipated that similar benefits would be achieved with more realistic boundary conditions. Neither panel design returned a critical buckling strain close to the maximum strain allowable imposed, given in Table 7, as the applied loading and fixed stiffener spacing in this numerical case do not generate high strains.

Panel Type	Stage	Panel Part	t	In-Plane			Out-Of-Plane			h_{st}	b_{fl}	b_{ext}
			(mm)	ξ_1^A	ξ_2^A	ξ_3^A	ξ_1^D	ξ_2^D	ξ_3^D	(mm)	(mm)	(mm)
Baseline	I	Stiffener flange	1.7	0.5000	0.4000	0.0000	0.3050	-0.3140	0.0000	44.9	35	-
		Skin	6.2	0.2318	-0.1281	0.0000	-0.0129	-0.9073	0.0000			
	II	Stiffener flange	2.156	0.2727	0.2727	0.0000	0.2186	-0.4846	0.1623	45	35	-
		Skin	6.272	0.2500	0.0000	0.0000	0.0537	-0.7500	-0.0439			
DST	I	Stiffener flange	4.2	0.5000	0.4000	0.0000	0.3050	-0.3140	0.0000	20.8	35	1
		Inner skin	3.1	-0.0004	-0.5920	0.0000	0.0187	-0.8461	0.0000			
		Outer skin	6.1	0.5778	0.5947	0.0000	0.8481	0.9223	0.0000			
	II	Stiffener flange	4.9	0.4400	0.3600	0.0000	0.3202	-0.2605	0.0092	21	35	1
		Inner skin	3.136	0.0000	-0.5000	0.0000	0.006	-0.9840	-0.0586			
		Outer skin	5.88	0.4667	0.4667	0.0000	0.4927	0.2865	-0.0284			

Table 5: Thicknesses, lamination parameters and structural widths for the optimum stiffened panel designs returned at the two stages of the optimisation routine.

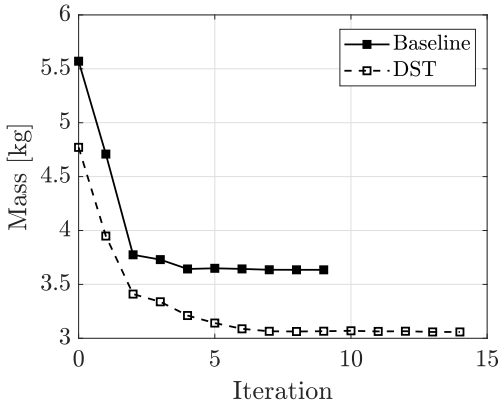

Figure 5: Stage I convergence plot for both panel designs.

Panel Type	Stacking Sequence (No. of Plies)	$0°/\pm45°/90°$ (%)	h_{st} (mm)	b_{st} (mm)	b_{ext} (mm)	Mass (kg)
Baseline	Stiffener flange $[\pm45/0_2/90/\overline{0}]_S$ (11 plies)	46/36/18	45	35	-	3.61
	Skin $[\mp45_3/\pm45/0/90/0_3/90/0_2]_S$ (32 plies)	37.5/50/12.5				
DST	Stiffener flange $[\pm45/0/\mp45/0_3/90/0_3/\overline{90}]_S$ (25 plies)	56/32/12	21	35	1	3.09
	Inner skin $[\mp45/\pm45/\mp45/0/90]_S$ (16 plies)	12.5/75/12.5				(-14.4%)
	Seam 1 $[\mp45/0/\pm45/0/\mp45/0/90]_S$ (20 plies)	30/60/10				
	Seam 2 $[\mp45/0_2/+45/90/0_2/\mp45/0/\overline{90}]_S$ (23 plies)	43.5/43.5/13				
	Seam 3 $[\mp45/0_3/+45/90/0_3/\mp45/0/\overline{90}]_S$ (27 plies)	52/37/11				
	Outer skin $[\mp45/0_4/90/0_4/90/\mp45/0]_S$ (30 plies)	60/27/13				

Table 6: Optimal final stacking sequence solutions for each panel type, with the respective standard angle percentages given for each layup. The final structural widths and the mass of one stiffener bay for each panel type are also presented.

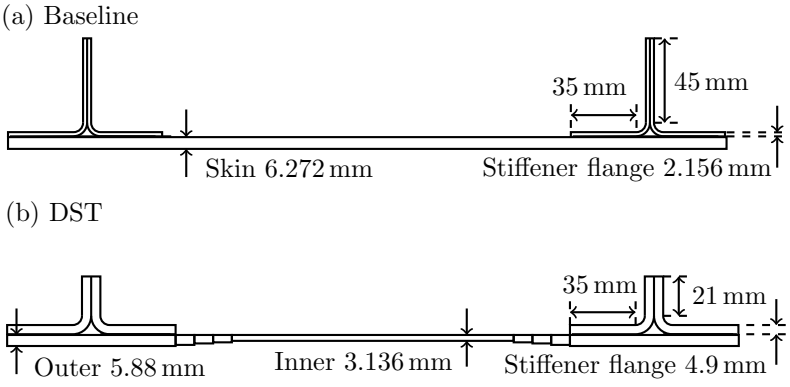

Figure 6: Cross-section comparison of the (a) Baseline and (b) DST optimum Stage II discrete designs.

Panel Type	Applied Load, P_x	Buckling Factors			Critical Buckling Strain, ϵ_x
	(kN)	Global	Skin	Stiffener	(µstrain)
Baseline	411.9	-	1.006	1.578	2177
DST	516.8	0.999	0.971	-	2310

Table 7: Theoretical VIPASA critical buckling factors (F_i) and strain values (ϵ_x) for the final discrete optimised designs.

6. Manufacture & Experimental Procedure

This section details the manufacture of the optimised DST panel from the previous numerical study and the testing process for the panel. Skin and stiffeners were formed and cured separately, then secondary bonded together using Redux liquid shim from Hexcel. The stiffeners were laid up using a custom aluminium mould and the stiffener noodles formed from rolled 0° prepreg, in line with current industrial practice [58]. The noodle region is indicated in Fig. 3. The skin panel was laid up on a steel plate which creates a flat surface to which the stiffeners are attached, and a stepped surface on the opposite side, as per Fig. 10b). This skin manufacturing procedure creates a cross-sectional geometry different to that modelled in the optimisation method and causes the position of the laminate neutral axis to vary across the width, and creates a stepped outer skin surface. It is noted that in this laboratory-scale test, the inner surface was manufactured as flat to facilitate bonding of the stiffeners to this surface. In reality, the outer surface of the skin would be used as the tool surface, with the step arising on the inner surface, as is necessary for optimal aerodynamic performance, but is not considered in this work. Some asymmetrical stacking sequences are present in the seam region, but these regions are very small in comparison to the full panel width, and no warping was seen post-cure. Once stiffeners were bonded, however, the finished panel skin was observed to have a small amount of positive out-of-plane curvature away from the stiffeners, measured at approximately 1 mm in amplitude over 600 mm of panel length and was therefore assumed to have developed during the secondary bonding process.

The final stiffener height (base to web top, including capping plies) was trimmed to 32 (+0.1) mm, the panel lengths and loading edges were machined to parallelism tolerances of 0.1 mm and 0.05 mm respectively, as suggested by Compression-After-Impact (CAI) composite standard test method ASTM D7137 [59] which is appropriated in the absence of a specific procedure. The fully manufactured panel was then potted in resin 25 mm deep at both loading edges, to avoid end brooming failure. The resin blocks were manufactured using a blend of Araldite 2011 A/ 2011 B/ HV997-1, 100:45:45 parts by weight. Although the creation of a clamped end condition is aided by these blocks, the true experimental boundary condition is indeterminate. As the strut-like global buckling factor for the DST case approaches one at the original design length L = 1000mm, in order to avoid this mode arising due to the uncertain end conditions, the experimental test panel length was shortened to 850 mm. The test panel length, accounting for the resin blocks, is therefore 800 mm. VIPASA results for a shortened panel length are also presented in Table 8. The buckling reserve factor for the L/2 half-wavelength is increased by 30% by shortening the panel length by 200 mm, however, the increase is not as significant as approximations using the Euler (strut)

buckling equation would suggest (+50%). The original (strut-like) global mode returned when $\lambda = L/2$ is no longer equivalent to the mode with $\lambda = L/2$ for the shorter panel which is dominated by plate-like buckling of the skin between stiffeners. The strut-like mode for the shorter panel will occur at a higher eigenvalue, and hence the results are not directly comparable. It is important to note that the post-buckling capacity is also artificially increased by shortening the panel.

	Applied Load	Panel Length	Buckling Factors			Critical Buckling Strain
Panel Type	P_x	L	Global*	Skin	Stiffener	ϵ_x
	(kN)	(mm)	($\lambda = L/2$)	($\lambda = L/6$)		(µstrain)
DST	516.8	1000	0.999 (strut)	0.971	-	2310
		800	1.296 (plate)	0.965	-	2296

Table 8: Theoretical VIPASA critical buckling factors (F_i) and strain values (ϵ_x) for the final DST design for alternative panel lengths. *Note that buckling for $\lambda = L/2$ changes to a skin-dominated plate mode as a result of the panel shortening.

A Dartec 2000 kN testing machine under displacement control was used to perform panel compression tests. Initial tests were run to 110% of the predicted buckling load at a displacement rate of 0.4 mm/min, and then a final test was conducted to failure. A speckle pattern was created on the front and back faces of the skin panel, and two pairs of low-speed stereo cameras were used for Digital Image Correlation (DIC) of the buckling modeshapes and surface strains. A pair of high speed DIC cameras were also used to capture the sudden failure of the panel. Thirteen pairs of axial strain gauges were employed to accurately determine the onset and development of buckling. A strain gauge map is shown in Fig 7f. Two transverse gauges, numbered 27 and 28, were placed either side of the seam transition to observe seam behaviour. Axial strain gauges were used to shim and correct the cross-head to ensure uniform loading across the panel. The gauges attached to the stiffener blade are placed approximately 3 mm from the free edge. The gauges are particularly useful for monitoring the stiffener webs as these are not captured by DIC.

7. Finite Element Analysis

Finite element analysis is conducted to provide validation of the optimised DST panel buckling load obtained using VIPASA, and for comparison with experimental results. A linear eigenvalue buckling analysis using a subspace solver is performed using the commercial software ABAQUS. The skin and stiffener are modelled using four-node general purpose shell elements (S4R) with three integration points within each ply, as these account for transverse shear which is likely to be influential due to laminate thicknesses considered [40]. The element size is in the region of 5 mm to guarantee the convergence of the first five modes to three significant figures. The stiffeners are attached to the skin using tie constraints to simulate bonding.

Replicating the experimental potted end conditions, the panel is restrained from displacement and rotation in all axes at one end, and all degrees of freedom except longitudinal displacements in the y-axis are restrained on the

loading edge as labelled in Fig. 3. Secondary tensile strains in the x-direction are therefore induced which results in a more conservative model than VIPASA, where no transverse loads are applied. The panel transverse edges are unconstrained. The load is applied as a uniform end shortening.

8. Results & Discussion

Plots of strain against compressive load, measured using the strain gauges, are shown in Fig. 7. Out-of-plane displacement plots obtained from DIC, illustrating the development of experimental modeshapes are presented in Fig 8. Analytical 2D buckling modeshapes determined using VIPASA and finite element analysis, along with an experimentally obtained modeshape are shown in Fig. 9. Cross-sectional plots of buckling modes, obtained from experimental DIC data are shown in Fig. 10.

Due to the pre-existing skin panel geometric imperfection, slight deviation of the upper strain gauges (15 & 22) on the 'Inner' skin region was observed from a load of 50 kN in Fig. 7d, indicating bending of the inner skin region, which is also recorded in the DIC z-displacement plots, Fig. 8a. The increased bending is restrained by the support of the stiffeners in the opposing direction, and the skin buckling is suppressed, before occurring at approximately 479 kN. Two experimental buckling modes are identified from the DIC analysis: a critical skin mode which developed initially, and a global mode which develops before the failure of the panel, presented in Fig 8c & f respectively. The onset of experimental buckling at 479 kN is evaluated from a change in gradient of the averaged 'Inner' skin gauges, given in Fig. 7a. From the averaged strain gauge results in Fig. 7 it can be seen that despite the onset of local skin buckling, there is no significant loss in the overall panel stiffness, not until a higher load where global mode is present and well developed. At a load of 536 kN, the experimental modeshape is composed of 4 full sinusoidal waves, confined to the 'Inner' skin region as observed in Figs. 9c & d. The centre of the panel developed a local modeshape as out-of-plane bending was already present due to the influence of the geometric imperfection, this is more clearly seen in the cross-section plot in Fig. 10. The analytically obtained modeshapes are highly comparable to each other as the shape is confined to the local buckling of the 'Inner' skin between the stiffeners, and both are composed of three full sine-waves down the length of the panel.

Analytical, FEA and experimental critical buckling loads, strains and the recorded overall axial stiffness of the panel are presented in Table 9. Comparing the stiffnesses, the FEA result is 8% more conservative than that obtained using VIPASA. This discrepancy is due to the difference in the applied boundary conditions, as transverse strains are induced in the FE analysis, promoting buckling at a lower load. The experimental buckling load of 479 kN is bounded by the VIPASA and FE results with differences of +3.8% and -4.8% respectively, which may be accounted for by geometric differences between the models and the actual manufactured design, the boundary conditions and premature experimental buckling due to the initial imperfection. Good agreement between the VIPASA and experimental results provides validation of the optimisation methodology which allows this approach to be applied to a study of stiffened panel designs, varying the stiffener spacing and compressive running loads, or to alternative structures.

A homogenised axial stiffness, obtained using Eq. (7), and a smeared panel thickness, were used to calculate

a stiffness of 70.4 GPa for the VIPASA model and FEA returns a similar but lower stiffness value of 69.5 GPa, as presented in Table 9. An experimental stiffness of 73.2 GPa was obtained from the initial gradient of the averaged skin panel strain gauges. Minor features, such as the noodle and the stiffener flange chamfer, exist in reality but were not initially modelled and contribute to the increased stiffness of the experimental panel.

Post the initial local skin mode, a global mode developed at approximately 536 kN which was determined through the distinct and significant divergence of the 'Inner' skin strain gauges (17 & 24) presented in Fig. 7d. The gradients of the lines before and after divergence are extrapolated, and the buckling load is taken from the point at which these intersect. The initiation of the global mode is also coincident with a discontinuous jump recorded at 542 kN in all strain gauges. The switch between modes is recorded in the DIC z-displacement plots captured at 536, 539 and 542 kN in Figs. 8c-e, as the local skin wavelengths are now integrated in a larger central buckle. Cross-sections in Fig. 10b show displacement across the width also suggesting a shift to a global mode after 542 kN. The strain gauges on the stiffener web presented in Fig 7b indicate that the stiffeners never buckle locally as predicted by the numerical study, but the stiffener webs mid-length are placed under significant compressive strain from the development of the large mid-length buckle due to the global mode.

Following global buckling, the panel was loaded until failure which occurred at a compressive load of 630 kN, 24% higher than the skin buckling load. Images from the high-speed cameras capturing the experimental panel failure are presented in Fig 11. Post-buckling, the compressive strain recorded by the mid-length stiffener web gauges (3 & 4 in Fig. 7b) increased significantly to approximately 6750 µstrain, and this consequently led to the compressive material failure of the left-hand stiffener web, as indicated in Fig. 11a. Crumpling of the left-hand stiffener resulted in fragmentation of the potted resin ends as labelled in Fig. 11a and the failure of the secondary bond between both stiffeners and the buckled skin panel, Figs. 11b & 11c. Post-test examination of both the debonded right-hand stiffener and skin panel found no clear outward signs of damage. However, it is impossible to establish the benefit of stiffness tailoring on post-buckling capacity as this is improved through shortening the panel length L to 800mm. It is noted that the transverse seam regions were able to carry the design load and a significant amount of post-buckling load to failure, for which the panel was not designed, without accruing visible damage. This underlines the potential benefit of DST despite the potential weakness of the transverse discontinuities.

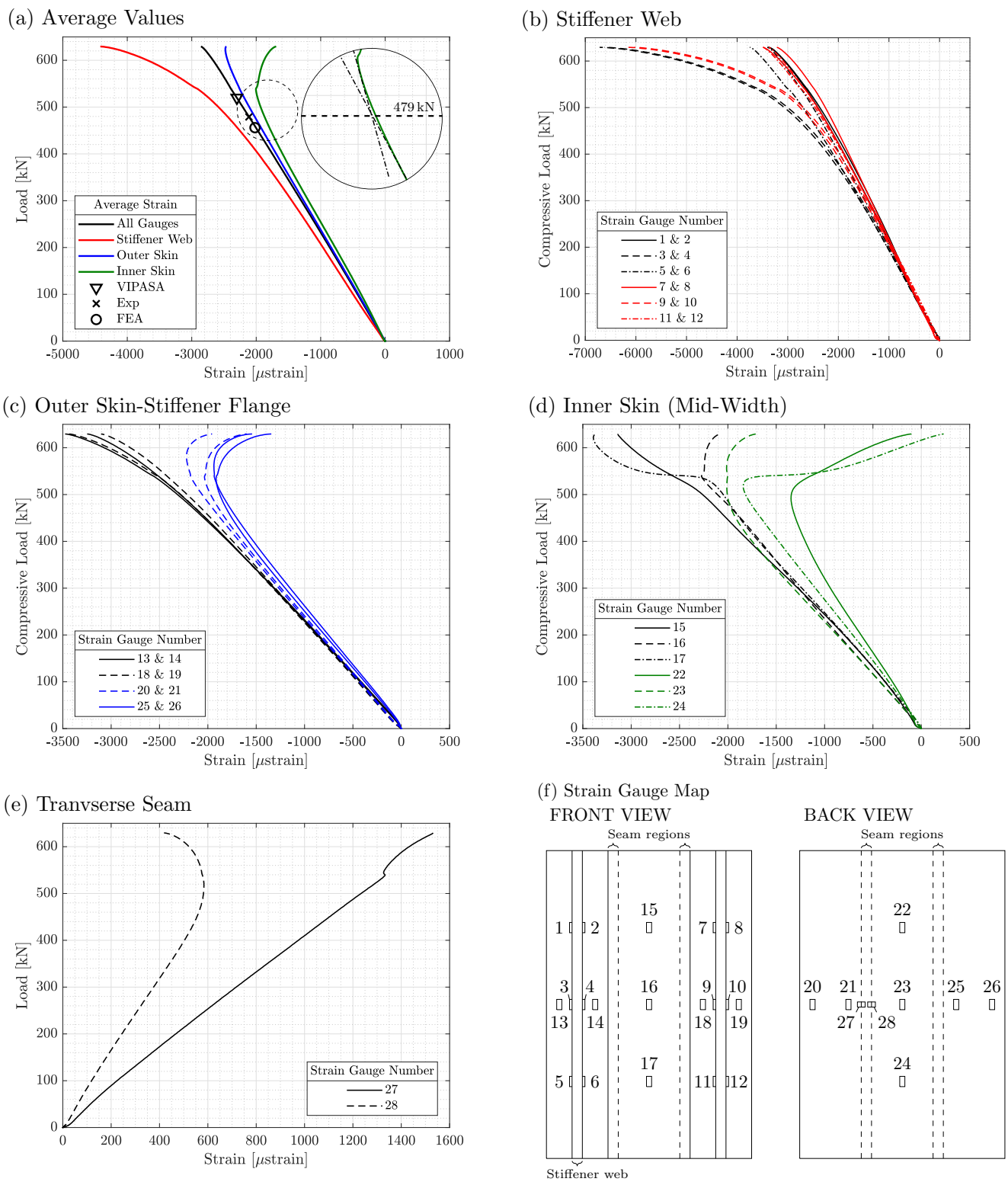

Figure 7: Strain vs compressive load. The strain gauge numbers in the legends correspond to the positions labelled on the strain gauge map.

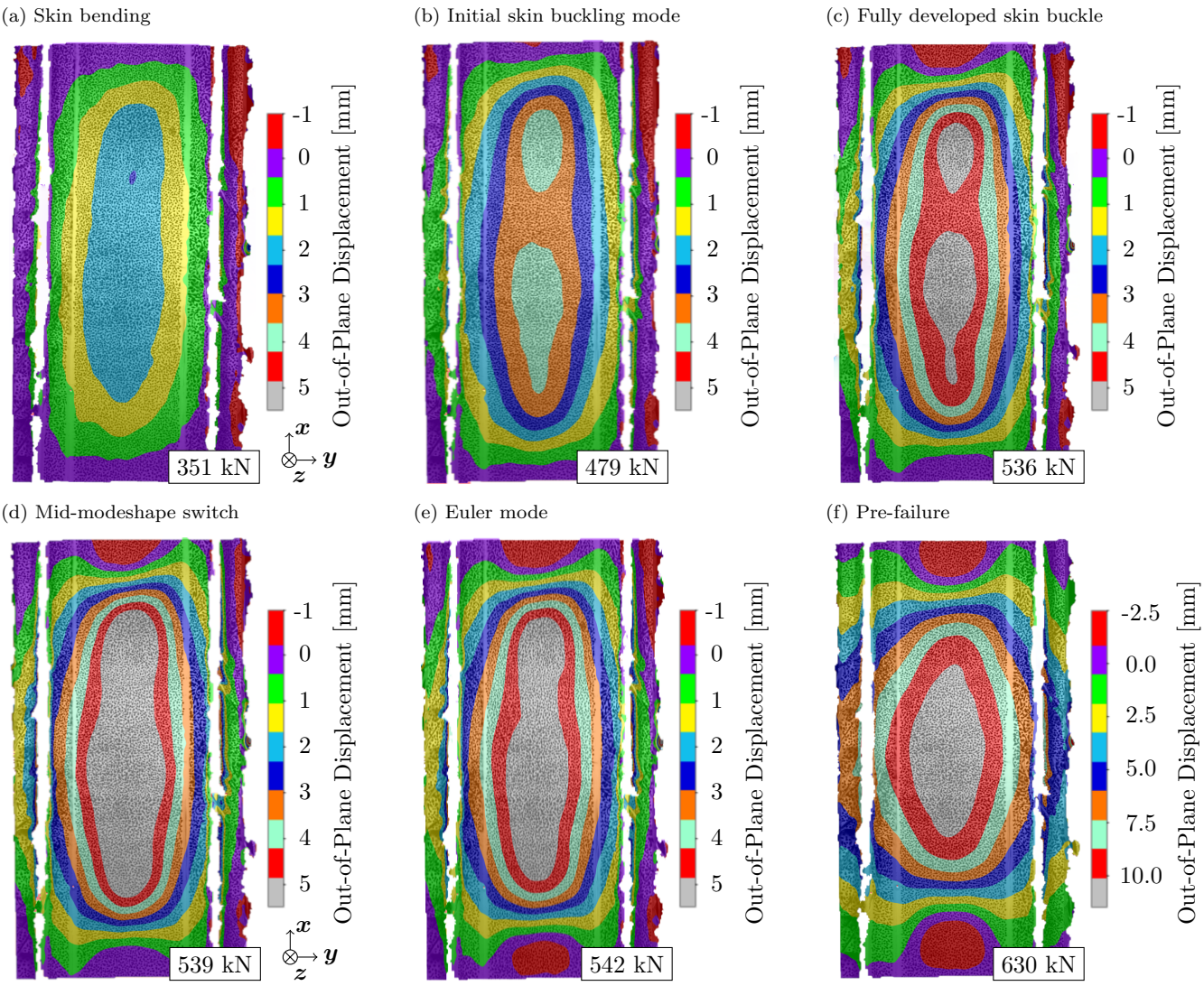

Figure 8: Out-of-plane displacements from the experimental test. Note that the sub-figure (f) has a different legend as the out-of-plane displacements are significantly larger.

	Exp.	VIPASA	FEA
Critical buckling load (kN)	479	498 (+3.8%)	456 (-4.8%)
Buckling strain (µstrain)	2113	2296	2008
E_{xx} (GPa)	73.2	69.3	69.5

Table 9: Comparison of experimental and analytical results for the DST stiffened panel design with a length of 800 mm and clamped boundary conditions.

(a) VIPASA: 498 kN (b) FE Analysis (c) Exp. Front Side: 536 kN (d) Exp. Back Side: 536 kN

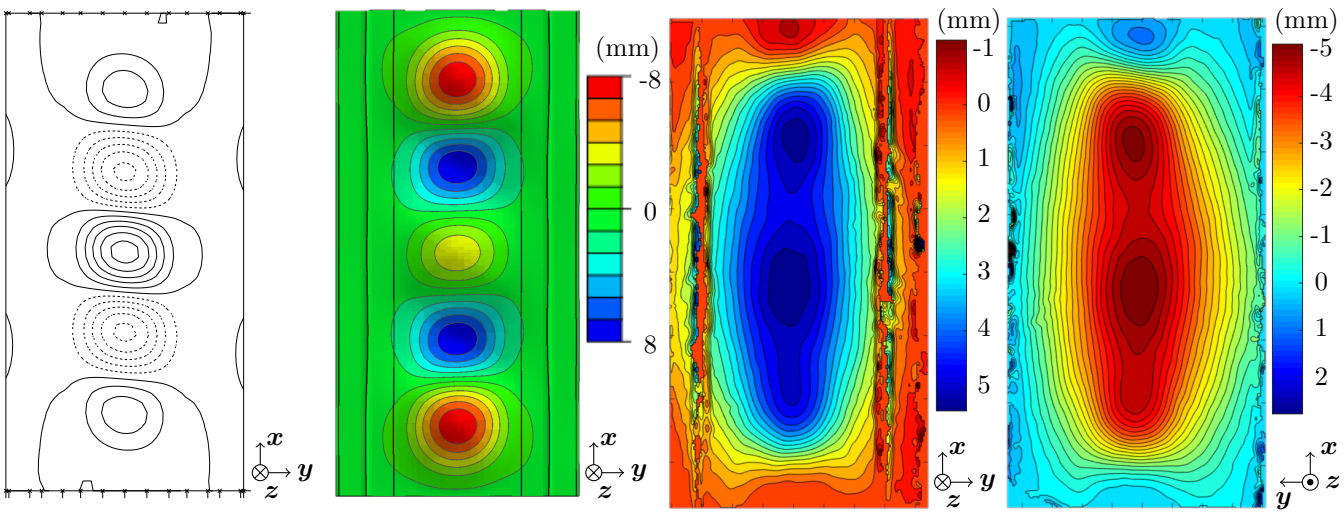

Figure 9: Comparison of 2D analytical and experimental buckling modeshapes. Red denotes negative z-displacement and blue represents positive z-displacement, consistent with labelled axes.

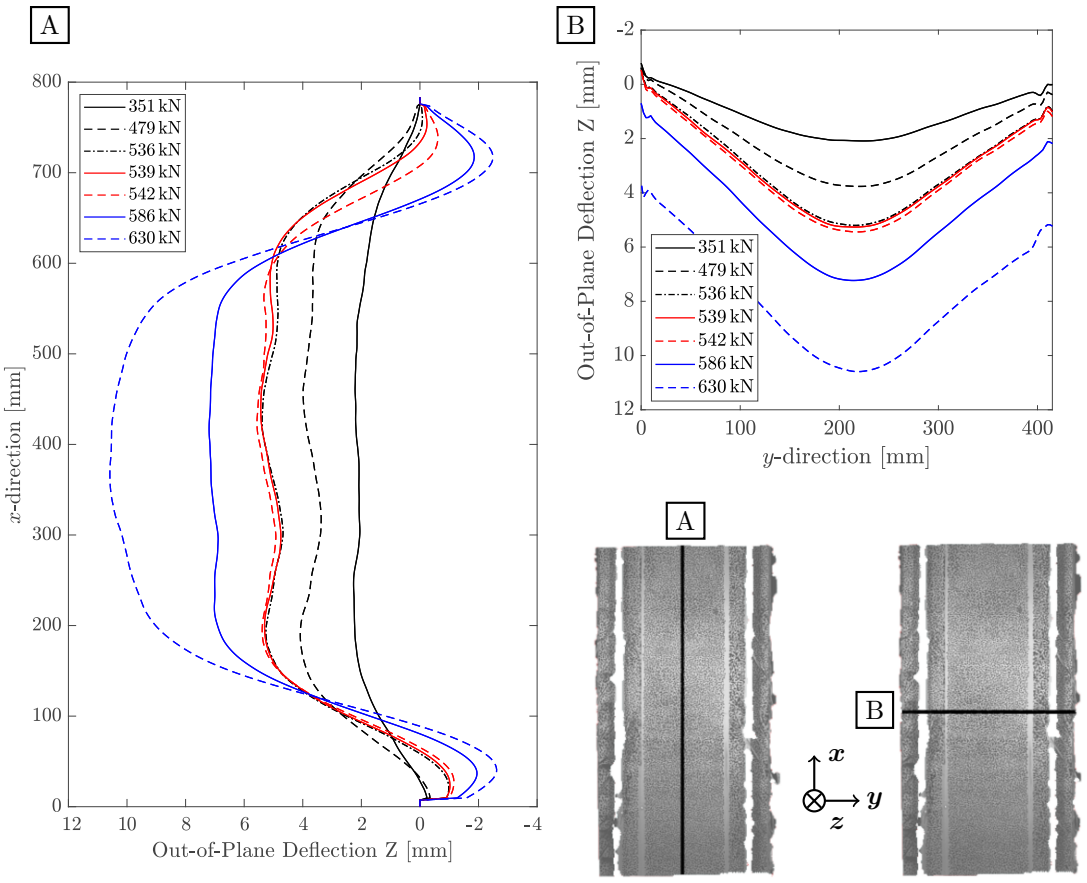

Figure 10: Out-of-plane displacement (Z) cross-section plots, showing development of the local skin and global modeshape with increased load. **A** is sampled from the xz plane, and **B** from the yz plane, and the position of the respective cutting planes are indicated on the panel diagrams.

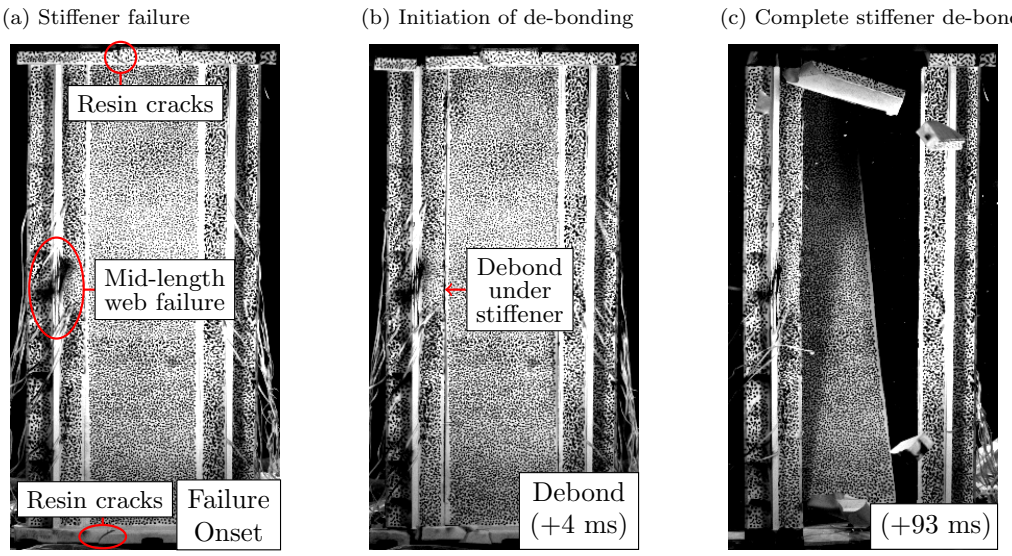

Figure 11: High-speed camera images of the panel failure at 630 kN. The initial failure of the left-hand mid length stiffener web is indicated, along with the cracking in the top and bottom resin potted ends.

9. Conclusion

In this paper, the novel concept of Discrete Stiffness Tailoring was presented as a means by which the optimal distribution of laminate stiffness and thickness can be achieved in order to realise easily manufacturable lower weight aerospace structures. An efficient two-stage optimisation methodology is employed, incorporating buckling and manufacturing constraints, and applied to produce a minimum mass discretely tailored stiffened compression panel.

- A 14.4% reduction in mass is obtained compared to a baseline constant stiffened case for a specific in-plane design load, when the tailoring philosophy is applied to the panel skin. Tailoring redistributes the load to the stiffener region, resulting in more efficient use of material.
- The optimised transition between the 'Outer' region, underneath the stiffener bond-line, and the 'Inner' free skin region is shown to occur immediately beneath the stiffener flange tip.
- DST is not constrained by a minimum fibre turning radius, which tend to be on the order of hundred of millimetres, a sharp transition can be effected.
- The optimised DST buckling load, obtained using the VIPASA model, was within 4% of that obtained experimentally. Good agreement between the analytical and experimental critical skin buckling modes was observed, although the experimental result was affected by a manufactured imperfection in the skin panel.
- Panel failure occurred at a load 24% greater than the skin buckling load, however as the panel length was shortened from the optimised design, the post-buckling capacity is increased.

- Failure was a result of material failure in the stiffener web. The seams within the tailored skin panel exhibited no sign of damage, despite the weak resin regions between the discontinuous plies, thus providing greater confidence in the transverse strength of a seamed region.

Acknowledgements

The authors would like to thank the EPSRC, GKN and Airbus for supporting the work carried out under the ADAPT project (EP/N024508/1). Lucie Culliford's PhD studentship is 50% funded by GKN Aerospace. Richard Butler holds a Royal Academy of Engineering - GKN Aerospace Research Chair. The authors would also like to acknowledge the technical help and expertise of Steven Thomas and William Bazeley at the University of Bath.

References

[1] S. B. Biggers, S. S. Pageau, Shear buckling response of tailored composite plates, AIAA Journal 32 (5) (1994) 1100–1103. doi:10.2514/3.12107.

[2] Z. Gürdal, B. F. Tatting, C. K. Wu, Variable stiffness composite panels: Effects of stiffness variation on the in-plane and buckling response, Composites Part A: Applied Science and Manufacturing 39 (5) (2008) 911–922. doi:10.1016/j.compositesa.2007.11.015.

[3] C. S. Lopes, Z. Gürdal, P. P. Camanho, Variable-stiffness composite panels: Buckling and first-ply failure improvements over straight-fibre laminates, Computers and Structures 86 (9) (2008) 897–907. doi:10.1016/j.compstruc.2007.04.016.

[4] M. W. Hyer, R. F. Charette, Use of curvilinear fiber format in composite structure design, AIAA Journal 29 (6) (1991) 1011–1015. doi:10.2514/3.10697.

[5] C. S. Lopes, Z. Gürdal, P. P. Camanho, Tailoring for strength of composite steered-fibre panels with cutouts, Composites Part A: Applied Science and Manufacturing 41 (12) (2010) 1760–1767. doi:10.1016/j.compositesa.2010.08.011.

[6] D. H. Lukaszewicz, C. Ward, K. D. Potter, The engineering aspects of automated prepreg layup: History, present and future, Composites Part B: Engineering 43 (3) (2012) 997–1009. doi:10.1016/j.compositesb.2011.12.003.

[7] G. G. Lozano, A. Tiwari, C. Turner, S. Astwood, A review on design for manufacture of variable stiffness composite laminates, Proceedings of the Institution of Mechanical Engineers, Part B: Journal of Engineering Manufacture 230 (6) (2016) 981–992. doi:10.1177/0954405415600012.

[8] B. C. Kim, K. Potter, P. M. Weaver, Continuous tow shearing for manufacturing variable angle tow composites, Composites Part A: Applied Science and Manufacturing 43 (8) (2012) 1347–1356. doi:10.1016/j.compositesa.2012.02.024.

[9] J. M. J. F. V. Campen, C. Kassapoglou, Z. Gürdal, Generating realistic laminate fiber angle distributions for optimal variable stiffness laminates, Composites Part B 43 (2) (2012) 354–360. doi:10.1016/j.compositesb.2011.10.014.

[10] D. M. Peeters, G. G. Lozano, M. M. Abdalla, Effect of steering limit constraints on the performance of variable stiffness laminates, Computers and Structures 196 (2018) 94–111. doi:10.1016/j.compstruc.2017.11.002.

[11] A. Crosky, C. Grant, D. Kelly, X. Legrand, G. Pearce, 4 - Fibre placement processes for composites manufacture, in: P. Boisse (Ed.), Advances in Composites Manufacturing and Process Design, Woodhead Publishing, 2015, pp. 79 – 92. doi:10.1016/B978-1-78242-307-2.00004-X.

[12] T. J. Dodwell, R. Butler, A. T. Rhead, Optimum fiber steering of composite plates for buckling and manufacturability, AIAA Journal 54 (3) (2016) 1139–1142. doi:10.2514/1.J054297.

[13] L. Culliford, R. Choudhry, R. Butler, A. Rhead, Buckling and strength analysis of panels with discrete stiffness tailoring, Composite Structures 234 (2020). doi:10.1016/j.compstruct.2019.111672.

[14] H. Ghiasi, K. Fayazbakhsh, D. Pasini, L. Lessard, Optimum stacking sequence design of composite materials Part II: Variable stiffness design, Composite Structures 93 (2010) 1–13. doi:10.1016/j.compstruct.2010.06.001.

[15] Z. Gürdal, R. Olmedo, In-plane response of laminates with spatially varying fiber orientations: Variable stiffness concept, AIAA Journal 31 (4) (1993) 751–758. doi:10.2514/3.11613.

[16] Z. Wu, P. M. Weaver, G. Raju, B. Chul Kim, Buckling analysis and optimisation of variable angle tow composite plates, Thin-Walled Structures 60 (2012) 163–172.

[17] L. Parnas, S. Oral, Ü. Ceyhan, Optimum design of composite structures with curved fiber courses, Composites Science and Technology 63 (7) (2003) 1071–1082. doi:10.1016/S0266-3538(02)00312-3.

[18] S. Nagendra, S. Kodiyalam, J. E. Davis, N. Parthasarathy, Optimization of tow fibre paths for composite design, in: 36th AIAA/ASME/ASCE/AHS/ASC Structure, Structural Dynamics and Materials Conference, no. 10-13 April, New Orleans, LA, 1995. doi:10.2514/6.1995-1275.

[19] B. P. Kristinsdottir, Z. B. Zabinsky, M. E. Tuttle, S. Neogi, Optimal design of large composite panels with varying loads, Composite Structures 51 (1) (2001) 93–102. doi:10.1016/S0263-8223(00)00128-8.

[20] B. Liu, R. T. Hafkta, Composite wing structural design optimization with continuity constraints, in: AIAA/ASME/ASCE/AHS/ASC Structures. Structural Dynamics, and Materials Conference, Seattle, WA, 2001.

[21] S. Tsai, N. Pagano, Invariant properties of composite materials, in: S. Tsai, H. J.C., N. Pagano (Eds.), Composite Materials Workshop, Stamfort Connecticut: Technomic Publishing Co., 1968, pp. 233–253.

[22] W. Tsai, Stephen, H. T. Hahn, Introduction to Composite Materials, CRC Press, 1980.

[23] H. Fukunaga, G. N. Vanderplaats, Stiffness optimization of orthotropic laminated composites using lamination parameters, AIAA Journal 29 (4) (1991) 641–646. doi:10.2514/3.59931.

[24] M. Miki, Y. Sugiyama, Optimum design of laminated composite plates using lamination parameters, AIAA Journal 31 (5) (1993) 921–922. doi:10.2514/3.49033.

[25] J. Grenestedt, P. Gudmundson, Layup optimization of composite material structures, in: P. Pedersen (Ed.), Optimal Design with Advanced Materials, Elsevier Science Publishers, Amsterdam, 1993, pp. 311–336.

[26] K. Yamazaki, Two-level optimization technique of composite laminate panels by genetic algorithms, 37th AIAA/ASME/ASCE/AHS/ASC Structure, Structural Dynamics and Materials Conference c (1996) 1882–1887. doi:10.2514/6.1996-1539.

[27] J. Enrique Herencia, P. M. Weavers, M. I. Friswell, Optimization of long anisotropic laminated fiber composite panels with T-shaped stiffeners, AIAA Journal 45 (10) (2007) 2497–2509. doi:10.2514/1.26321.

[28] D. Liu, V. V. Toropov, O. M. Querin, D. C. Barton, Bilevel optimization of blended composite wing panels, Journal of Aircraft 48 (1) (2011) 107–118. doi:10.2514/1.C000261.

[29] T. Macquart, N. Werter, R. De Breuker, Aeroelastic design of blended composite structures using lamination parameters, Journal of Aircraft 54 (2) (2017) 561–571. doi:10.2514/1.C033859.

[30] S. T. IJsselmuiden, M. M. Abdalla, O. Seresta, Z. Gürdal, Multi-step blended stacking sequence design of panel assemblies with buckling constraints, Composites Part B: Engineering 40 (4) (2009) 329–336. doi:10.1016/j.compositesb.2008.12.002.

[31] M. Autio, Determining the real lay-up of a laminate corresponding to optimal lamination parameters by genetic search, Structural and Multidisciplinary Optimization 20 (4) (2000) 301–310. doi:10.1007/s001580050160.

[32] Z. Wu, G. Raju, P. M. Weaver, Framework for the buckling optimization of variable-angle tow composite plates, AIAA Journal 53 (12) (2015) 3788–3804. doi:10.2514/1.J054029.

[33] P. Hao, X. Yuan, C. Liu, B. Wang, H. Liu, G. Li, F. Niu, An integrated framework of exact modeling, isogeometric analysis and optimization for variable-stiffness composite panels, Computer Methods in Applied Mechanics and Engineering 339 (2018) 205–238. doi:10.1016/j.cma.2018.04.046.
URL https://doi.org/10.1016/j.cma.2018.04.046

[34] P. Hao, D. Liu, Y. Wang, X. Liu, B. Wang, G. Li, S. Feng, Design of manufacturable fiber path for variable-stiffness panels based on lamination parameters, Composite Structures 219 (January) (2019) 158–169. doi:10.1016/j.compstruct.2019.03.075.
URL https://doi.org/10.1016/j.compstruct.2019.03.075

[35] G. Serhat, I. Basdogan, Lamination parameter interpolation method for design of manufacturable variable-stiffness composite panels, AIAA Journal 57 (7) (2019) 3052–3065. doi:10.2514/1.J057902.

[36] B. G. Falzon, G. P. Steven, Buckling mode transition in hat-stiffened composite panels loaded in uniaxial compression, Composite Structures 37 (2) (1997) 253–267. doi:10.1016/S0263-8223(97)80017-7.

[37] R. Vescovini, C. Bisagni, Buckling analysis and optimization of stiffened composite flat and curved panels, AIAA Journal 50 (4) (2012) 904–915. doi:10.2514/1.J051356.

[38] B. H. Coburn, Z. Wu, P. M. Weaver, Buckling analysis of stiffened variable angle tow panels, Composite Structures 111 (1) (2014) 259–270. doi:10.1016/j.compstruct.2013.12.029.
URL http://dx.doi.org/10.1016/j.compstruct.2013.12.029

[39] S. Nagendra, Z. Gürdal, R. T. Haftka, J. H. Starnes, Buckling and failure characteristics of compression-loaded stiffened composite panels with a hole, Composite Structures 28 (1) (1994) 1–17. doi:10.1016/0263-8223(94)90002-7.

[40] W. Liu, R. Butler, A. R. Mileham, A. J. Green, Bilevel optimization and postbuckling of highly strained composite stiffened panels, AIAA Journal 44 (11) (2006) 2562–2570. doi:10.2514/1.22206.

[41] A. Sabido, L. Bahamonde, R. Harik, M. J. van Tooren, Maturity assessment of the laminate variable stiffness design process, Composite Structures 160 (2017) 804–812. doi:10.1016/j.compstruct.2016.10.081.

[42] C. Wu, Z. Gurdal, J. Starnes, Structural Response of Compression-Loaded, Tow-Placed, Variable Stiffness Panels, in: AIAA/ASME/ASCE/AHS/ASC Structures. Structural Dynamics, and Materials Conference, no. 22-25 April, 2002. doi:10.2514/6.2002-1512.

[43] D. C. Jegley, B. F. Tatting, Z. Gürdal, Tow-steered panels with holes subjected to compression or shear loading, Collection of Technical Papers - AIAA/ASME/ASCE/AHS/ASC Structures, Structural Dynamics and Materials Conference 5 (2005) 3453–3466. doi:10.2514/6.2005-2081.

[44] P. M. Weaver, K. D. Potter, K. Hazra, M. A. Saverymuthapulle, M. T. Hawthorne, Buckling of variable angle tow plates: From concept to experiment, Collection of Technical Papers - AIAA/ASME/ASCE/AHS/ASC Structures, Structural Dynamics and Materials Conference (May) (2009) 1–10. doi:10.2514/6.2009-2509.

[45] V. Oliveri, G. Zucco, D. Peeters, G. Clancy, R. Telford, M. Rouhi, C. McHale, R. M. O'Higgins, T. M. Young, P. M. Weaver, Design, manufacture and test of an in-situ consolidated thermoplastic variable-stiffness wingbox, AIAA Journal 57 (4) (2019) 1671–1683. doi:10.2514/1.J057758.

[46] T. R. Brooks, J. R. Martins, G. J. Kennedy, High-fidelity aerostructural optimization of tow-steered composite wings, Journal of Fluids and Structures 88 (2019) 122–147. doi:10.1016/j.jfluidstructs.2019.04.005.

[47] C. Y. M. Niu, Composite Airframe Structures: Practical Design Information and Data, Conmilit, Hong Kong, 1992.

[48] W. H. Wittrick, F. W. Williams, Buckling and vibration of anisotropic or isotropic plate assemblies under combined loadings, International Journal of Mechanical Sciences 16 (4) (1974) 209–239. doi:10.1016/0020-7403(74)90069-1.

[49] W. H. Wittrick, General sinusoidal stiffness matrices for buckling and vibration analyses of thin flat-walled structures, International Journal of Mechanical Sciences 10 (12) (1968) 949–966. doi:10.1016/0020-7403(68)90049-0.

[50] W. Wittrick, F. Williams, A general algorithm for computing natural frequencies of elastic structures, The Quarterly Journal of Mechanics and Applied Mathematics 24 (3) (1971) 263–284.

[51] C. G. Diaconu, H. Sekine, Layup optimization for buckling of laminated composite shells with restricted layer angles, AIAA Journal 42 (10) (2004) 2153–2163. doi:10.2514/1.931.

[52] J. E. Herencia, P. M. Weaver, M. I. Friswell, Initial sizing optimisation of anisotropic composite panels with T-shaped stiffeners, Thin-Walled Structures 46 (4) (2008) 399–412. doi:10.1016/j.tws.2007.09.003.

[53] B. Liu, R. T. Haftka, P. Trompette, Maximization of buckling loads of composite panels using flexural lamination parameters, Structural and Multidisciplinary Optimization 26 (1-2) (2004) 28–36. doi:10.1007/s00158-003-0314-7.

[54] M. M. Abdalla, C. Kassapoglou, Z. Gürdal, Formulation of composite laminate robustness constraint in lamination parameters space, Collection of Technical Papers - AIAA/ASME/ASCE/AHS/ASC Structures, Structural Dynamics and Materials Conference (May) (2009) 1–15. doi:10.2514/6.2009-2478.

[55] K. He, S. V. Hoa, R. Ganesan, The study of tapered laminated composite structures: A review, Composites Science and Technology 60 (14) (2000) 2643–2657. doi:10.1016/S0266-3538(00)00138-X.

[56] R. T. Haftka, J. L. Walsh, Stacking-sequence optimization for buckling of laminated plates by integer programming, AIAA Journal 30 (3) (1992) 814–819. doi:10.2514/3.10989.

[57] O. Falcó, J. A. Mayugo, C. S. Lopes, N. Gascons, A. Turon, J. Costa, Variable-stiffness composite panels: As-manufactured modeling and its influence on the failure behavior, Composites Part B: Engineering 56 (2014) 660–669. doi:10.1016/j.compositesb.2013.09.003.

[58] Z. Sápi, R. Butler, A. Rhead, High fidelity analysis to predict failure in T-joints, Composite Structures 225 (February) (2019) 111143. doi:10.1016/j.compstruct.2019.111143.

[59] American Society for Testing and Materials International. Standard test for compressive residual strength properties of damaged polymer matrix composite plates. ASTM D7137/D7137M-07.